LETTER

doi:10.1038/nature14128

Optogenetic control of organelle transport and positioning

Petra van Bergeijk[1]*, Max Adrian[1]*, Casper C. Hoogenraad[1] & Lukas C. Kapitein[1]

Proper positioning of organelles by cytoskeleton-based motor proteins underlies cellular events such as signalling, polarization and growth[1–8]. For many organelles, however, the precise connection between position and function has remained unclear, because strategies to control intracellular organelle positioning with spatiotemporal precision are lacking. Here we establish optical control of intracellular transport by using light-sensitive heterodimerization to recruit specific cytoskeletal motor proteins (kinesin, dynein or myosin) to selected cargoes. We demonstrate that the motility of peroxisomes, recycling endosomes and mitochondria can be locally and repeatedly induced or stopped, allowing rapid organelle repositioning. We applied this approach in primary rat hippocampal neurons to test how local positioning of recycling endosomes contributes to axon outgrowth and found that dynein-driven removal of endosomes from axonal growth cones reversibly suppressed axon growth, whereas kinesin-driven endosome enrichment enhanced growth. Our strategy for optogenetic control of organelle positioning will be widely applicable to explore site-specific organelle functions in different model systems.

Eukaryotic cells use cytoskeletal motor proteins to control the transport and positioning of proteins, RNAs and organelles[1]. In neurons, mitochondria positioning contributes to synapse functioning and axon branching[2,7,8], whereas positioning of Golgi outposts is thought to control dendrite development[6]. Likewise, specific positioning of endosomes has been proposed to contribute to polarization and local outgrowth, either through selective delivery of building blocks or through localized signalling[5,9–12]. In many cases, however, directly resolving the role of specific organelle positioning has remained challenging. Disruption of cytoskeletal elements and inhibition of motor proteins or adaptor molecules have been frequently used to alter organelle positioning, but these approaches often lack target selectivity as well as spatial specificity. Therefore, a tool to modulate locally the distribution of specific organelles with spatiotemporal accuracy is required.

Using light-induced heterodimerization to recruit specific motors to selected cargoes might enable spatiotemporal control of intracellular transport, but whether such light-induced interactions can withstand motor-induced forces has remained unclear[13,14]. To test this, we first used light-induced binding to couple microtubule-based motors to peroxisomes in monkey COS-7 cells, because these vesicular organelles are largely immobile in the perinuclear region and any movement induced by light-targeted motor proteins could easily be observed[15]. Peroxisomes were labelled using PEX–LOV, a fusion between the peroxisomal targeting signal of PEX3 and a photosensitive LOV domain from *Avena sativa* phototropin 1, which cages a small peptide that binds the engineered PDZ domain ePDZb1 after exposure to blue light[14] (Fig. 1a, b). In addition, ePDZb1 was fused to the plus-end-directed kinesin-3 KIF1A to create KIF–PDZ. After co-expression of these two constructs and illumination with blue light, we observed the rapid redistribution of peroxisomes from the centre to the periphery of the cell where most microtubule plus-ends are located (Fig. 1c, d). Similarly, light-induced recruitment of minus-end-directed dynein using the amino terminus of BICD2 (BICDN) fused to ePDZb1 (BICDN–PDZ) triggered the accumulation of peroxisomes at the centre of the cells (Extended Data Fig. 1a–c and Supplementary Video 1). Importantly, peroxisome redistribution did not alter the spatial organization of mitochondria, the endoplasmic reticulum, or the actin and microtubule cytoskeleton (Extended Data Fig. 2a, b).

To quantify peroxisome motility, we first used image correlation analysis to measure the overall frame-to-frame similarity before and after exposure to blue light[16]. In the absence of transport, two subsequent images are largely identical and the correlation index will be close to 1, whereas a value of 0 indicates that all organelles have moved to previously unoccupied positions. After light-induced recruitment of KIF1A, the correlation index rapidly decreased from 0.97 ± 0.01 (mean ± s.e.m.)

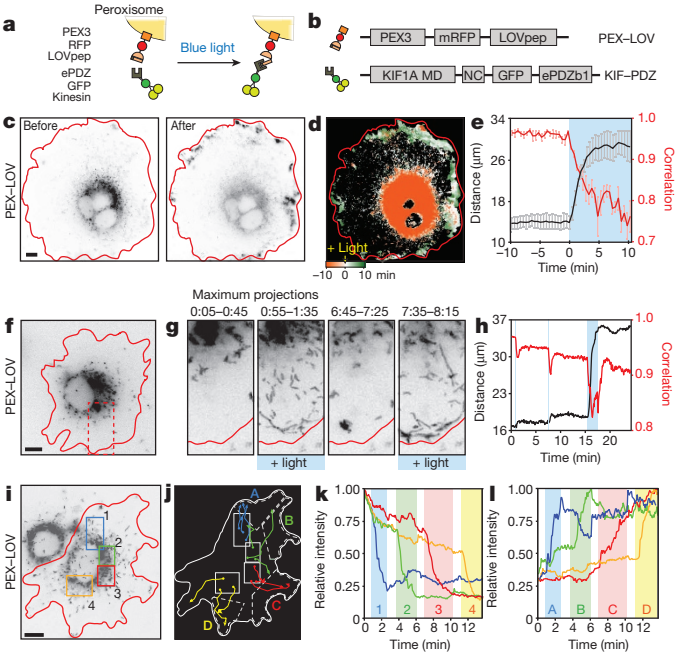

Figure 1 | Local and reversible activation of microtubule-based transport with light. **a**, **b**, Assay and constructs. MD, motor domain; NC, neck coil. **c**, Peroxisome distribution before and after light-induced recruitment of KIF–PDZ. **d**, Colour-coded overlay of time series. **e**, Displacement (black, expressed in $R_{90\%}$) and correlation (frame-to-frame similarity from 0 to 1, red) versus time ($n = 6$ cells, mean ± s.e.m.). Blue marks illumination. **f**, **g**, Reversible activation using pulsed light. **g**, Maximum intensity projections during periods of 40 s. See Supplementary Video 2. Time shown in minutes:seconds. **h**, Displacement (black, $R_{90\%}$) and correlation (red) versus time. **i**–**l**, Local activation using sequential illumination of four regions (**i**), resulting in outward targeting to adjacent regions (**j**, showing example trajectories), quantified using normalized fluorescence intensity (**k**, **l**, coloured boxes mark blue-light illumination). See Supplementary Video 3. Scale bars, 10 μm.

[1]Cell Biology, Department of Biology, Faculty of Science, Utrecht University, 3584 CH Utrecht, The Netherlands.
*These authors contributed equally to this work.

to 0.76 ± 0.04, reflecting the induction of continuous peroxisome motility (Fig. 1e). By contrast, dynein recruitment eventually increased the correlation index, because most peroxisomes accumulated at the same position in the centre of the cell (Extended Data Fig. 1c, d). To quantify this overall peroxisome repositioning, we calculated for each time point the radius of the circle required to enclose 90% of the fluorescence intensity of the peroxisomes, $R_{90\%}$, and found a large increase from 14 ± 2 μm to 29 ± 3 μm on recruitment of KIF1A (Fig. 1e). By contrast, $R_{90\%}$ decreased from 15.4 ± 0.3 μm to 12.8 ± 0.6 μm on recruitment of dynein (Extended Data Fig. 1d). Thus, rapid organelle redistribution can be induced by using light to recruit microtubule motors.

To achieve spatiotemporal control, recruitment of motors should be both reversible and locally restricted. To test the reversibility of motility induction, we exposed cells expressing KIF–PDZ and PEX–LOV to three consecutive periods of blue light, interspersed with ~7 min without blue-light exposure. Whereas peroxisomes moved outwards during blue-light illumination, movement was arrested within seconds without blue light (Fig. 1f, g and Supplementary Video 2). By contrast, $R_{90\%}$ remained stable without stimulation (Fig. 1h), indicating that peroxisomes do not spontaneously return to their original position after motor dissociation (Extended Data Fig. 3a). To test whether transport could be induced locally, we sequentially illuminated four different regions within a cell (Fig. 1i, j). Peroxisomes in the activated region rapidly redistributed to non-exposed areas, whereas non-exposed peroxisomes remained stationary (Fig. 1j and Supplementary Video 3). The fluorescence intensity in the illuminated boxes 1–4 decreased by 60–75%, coinciding with a 180–280% increase in the adjacent peripheral boxes A–D (Fig. 1j–l). These results demonstrate that transport of intracellular cargo can be induced with spatiotemporal precision.

We have previously shown that myosin-V can oppose kinesin-driven transport in actin-dense regions[16], suggesting that light-induced recruitment of myosin-V can be used to anchor organelles at specific sites. To test this, myosin-Vb was recruited to peroxisomes preloaded with the kinesin-2 KIF17 (refs 15, 16) (Fig. 2a, b). Whereas the attached kinesin motor ensured continuous motility of many peroxisomes near the cell periphery (Fig. 2c), this motility was arrested after recruitment of myosin-Vb, resulting in a 30% increase of the correlation index (Fig. 2d). Local illumination increased the correlation index to similar levels, but only in the exposed region (Fig. 2c, d). Moreover, individual peroxisome trajectories showed on average four times smaller frame-to-frame displacements during illumination compared to before and after stimulation (Fig. 2e, f). These data demonstrate that organelle motility can be stalled with spatiotemporal precision through light-induced recruitment of myosin-Vb.

We next used RAB11-positive recycling endosomes to test our method on organelles whose proper physiological functioning depends on selective transport and positioning. Kinesin- and dynein-based redistribution and myosin-Vb-based anchoring of recycling endosomes could be transiently induced with light (Extended Data Figs 2–4, see also Supplementary Information, Extended Data Figs 5 and 6 and Supplementary Videos 4 and 5), demonstrating that the movement of intrinsically dynamic cargoes can be temporarily amplified or overruled by coupling these cargoes to a specific motor using light. Notably, whereas peroxisomes remained largely immobile at their new location after light-dependent repositioning, the original distribution of recycling endosomes was quickly restored after the light-induced kinesin recruitment was stopped (Extended Data Fig. 3).

To test our approach in a more complex and delicate model system, we switched to primary cultures of rat hippocampal neurons. Their polarized morphology and specialized cytoskeletal organization in different compartments, such as axons, dendrites and dendritic spines, should allow transporting cargoes into and out of these compartments by recruiting the appropriate motor proteins. We first examined whether light-induced recruitment of myosin-Vb was sufficient to drive transport into dendritic spines, as proposed previously[17–20]. Indeed, in cells co-expressing PEX–LOV and a fusion of myosin-Vb with ePDZb1 (MYO–PDZ), 62 ± 3% of the illuminated spines were targeted with peroxisomes compared to 1 ± 1% of spines in non-illuminated dendrites (Fig. 2g–j and Supplementary Video 6). After the illumination period, the number of peroxisome entries decreased with a half-time of ~36 s (Fig. 2j).

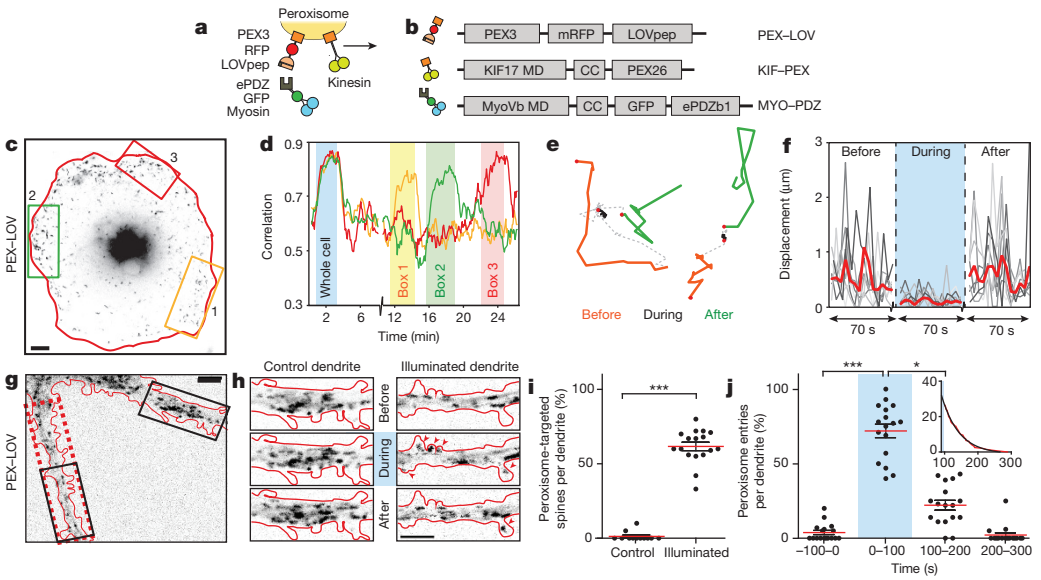

Figure 2 | Light-induced myosin-Vb recruitment anchors organelles or targets them into dendritic spines. **a**, **b**, Assay and constructs. CC, coiled coil. **c**, Peroxisome distribution in cell expressing PEX–LOV, KIF–PEX and MYO–PDZ. **d**, Correlation time trace for areas shown in **c**. **e**, Peroxisome trajectories with 70-s episodes before, during and after myosin-Vb recruitment. **f**, Frame-to-frame displacements of peroxisomes (5 s interval). Red denotes the average of nine individual peroxisome trajectories. **g**, Peroxisome distribution in primary hippocampal neuron expressing PEX–LOV and MYO–PDZ. Dashed red rectangle was illuminated. **h**, Thirty-second maximum projections of regions from **g**. Arrowheads mark peroxisomes in spines. See Supplementary Video 6. **i**, Spine targeting in control ($n = 12$) and illuminated ($n = 17$) dendrites, in three independent experiments. Mean ± s.e.m., $***P < 0.0001$, Mann–Whitney test. **j**, Spine entries over time. Mean ± s.e.m., $*P < 0.05$, $***P < 0.0001$, Kruskal–Wallis analysis of variance (ANOVA), Dunn's post-hoc test, $n = 17$ dendrites. Inset: entry probability after illumination (red) fitted with exponential decay $\exp(t\,\lambda^{-1})$ (black, $\lambda = 36.36$ s). Scale bars, 5 μm (**g**, **h**) and 10 μm (**c**).

Similarly, RAB11 recycling endosomes could be enriched in specific spines by local illumination (Extended Data Fig. 4o–q), demonstrating that light-controlled transport can be used to manipulate individual dendritic spines.

RAB11 vesicles have been implicated in the control of axon growth, but their local role in the growth cone could not be assessed previously[11,12,21]. We therefore used local light-induced recruitment of motor proteins to RAB11 recycling endosomes to test how local dynein-driven removal or kinesin-driven addition of endosomes affects growth cone dynamics (Fig. 3a, d). Importantly, neither illumination nor addition of the heterodimerizer rapalog (used to link the LOV domain to the N terminus of RAB11) altered growth cone structure or behaviour in cells expressing FRB–LOV and PDZ only (Extended Data Figs 5 and 7). Likewise, in control neurons expressing FKBP–RAB11 together with BICDN–PDZ or KIF–PDZ, but lacking the FRB–LOV protein, exposure to blue light did not affect the rapid filopodial and lamellipodial dynamics or the overall growth of most growth cones. (Fig. 3b, e). When dynein was coupled to RAB11, a clear decrease in growth cone dynamics and growth was observed (Fig. 3c, g, Extended Data Fig. 8 and Supplementary Video 7). By contrast, coupling of kinesin resulted in rapid axon extension in 39 ± 7% of the growth cones (Fig. 3f, h and Supplementary Video 7). Importantly, when growth cones were not completely collapsed upon dynein-dependent RAB11 depletion, this depletion and the reduced growth cone dynamics could be reversed when cells were no longer exposed to blue light (Fig. 3i, j). These data demonstrate that growth cone dynamics and axon growth directly depend on RAB11 vesicle functioning near the growth cone, rather than on general RAB11 functions elsewhere in the cell.

Recently, the controlled anchoring and mobilization of mitochondria have emerged as key regulatory events in neurons[8,22–24]. Mitochondrial positioning depends on both motor-dependent transport and controlled immobilization by specific docking factors, but the molecular and mechanical interplay between motors and docking factors has remained unclear[22,24]. For example, syntaphilin (SNPH) has been proposed to induce anchoring by crosslinking mitochondria to microtubules and through a direct inactivating interaction with kinesin[25,26], but whether remobilization requires the regulated release of both interactions is not known[23]. To test whether recruitment of more motors can overcome anchoring, we used light to recruit KIF–PDZ to axonal mitochondria labelled with TOM–LOV (Fig. 4a, b) and found that this was sufficient to mobilize most mitochondria in the illuminated region (Fig. 4c–g and Supplementary Video 8). Conversely, light-induced recruitment of the N-terminal part of SNPH was sufficient to acutely anchor motile mitochondria, independent of their directionality (Fig. 4h–j and Supplementary Video 9). These results demonstrate that regulation of mitochondrial motility and anchoring does not require all-or-nothing switching between the activation and inactivation of specific motors, but instead depends on the balance of forces between active motors and passive anchors.

We have established optically-controlled intracellular transport by using light-sensitive heterodimerization to recruit specific cytoskeletal motor proteins to selected cargoes. Our ability to control organelle positioning complements recent work that established optogenetic control over nucleocytoplasmic distribution of proteins[27]. We anticipate that this approach will be widely applicable to study how organelle positioning controls cellular functioning, as demonstrated here for the role

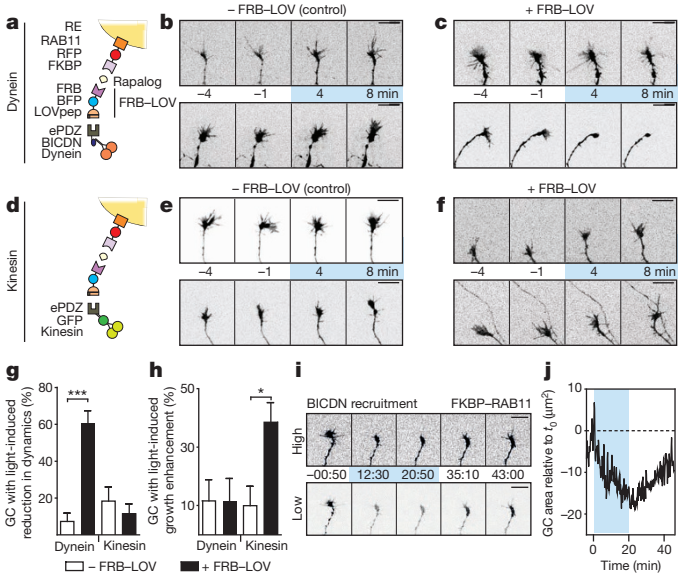

Figure 3 | Motor-based redistribution of recycling endosomes modulates axon outgrowth. **a**, **d**, Assay and constructs. Rapalog targets FRB–LOV to the RAB11 N terminus. **b**, **c**, **e**, **f**, Growth cone dynamics of neurons expressing FKBP–RAB11 and BICDN–PDZ (**b**, **c**) or KIF–PDZ (**e**, **f**) without (**b**, **e**) or with (**c**, **f**) FRB–LOV. See Supplementary Video 7. **g**, **h**, Light-induced reduction of growth cone (GC) dynamics (**g**) or light-induced growth enhancement (**h**). Dynein/kinesin: −FRB–LOV: $n = 21/19$ axons, +FRB–LOV: $n = 25/35$ axons, in $n = 5/5$ independent experiments. Mean ± s.e.m., $^*P < 0.05$, $^{***}P < 0.0001$, unpaired two-tailed t-test. **i**, Same growth cone in low and high contrast illustrating reversibility of reduced FKBP–RAB11 targeting and growth cone dynamics. **j**, Area over time for the example shown in **i**. Scale bars, 10 μm.

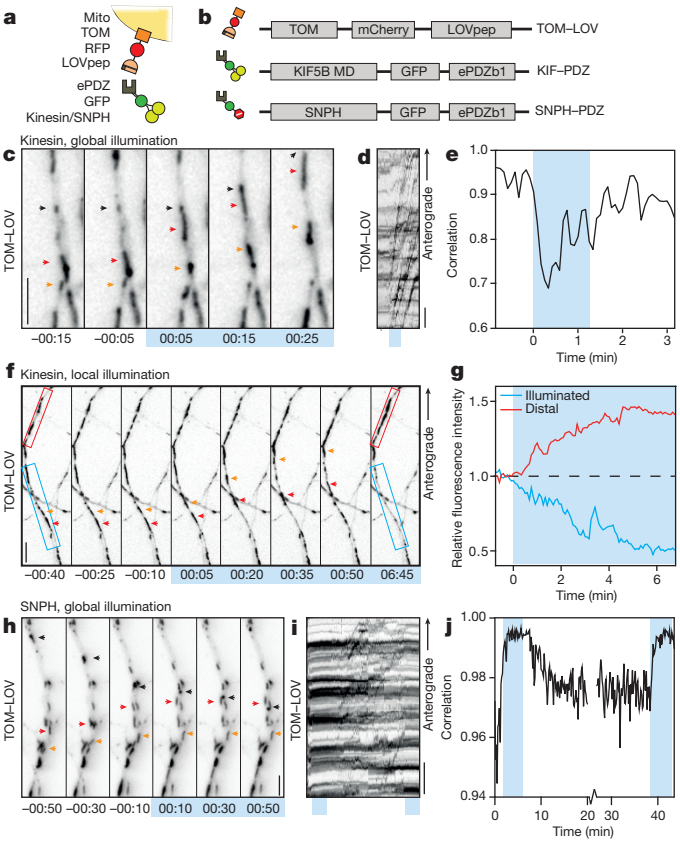

Figure 4 | Altering mitochondrial dynamics through recruitment of motors and anchors. **a**, **b**, Assay and constructs. **c**, Axonal mitochondria before and during KIF–PDZ recruitment. Arrowheads track individual mitochondria. See Supplementary Video 8. **d**, Kymograph for axon shown in **c**, representative for $n = 6$ axons. Blue box marks activation (1 min:15 s). **e**, Correlation over time for region shown in **c**. **f**, Axonal mitochondria before and during local illumination (blue box). See Supplementary Video 8. **g**, Relative fluorescence intensity versus time in the illuminated (blue box in **f**) and the adjacent, distal region (red box in **f**). **h**, Axonal mitochondria before and during SNPH recruitment. Arrowheads track individual mitochondria. See Supplementary Video 9. **i**, Kymograph for axon shown in **h**, representative for $n = 5$ axons. Blue boxes mark activation (4 min:50 s). **j**, Correlation versus time for region in Supplementary Video 9. Scale bars, 5 μm (**c**, **f**, **h**) and 10 μm (**d**, **i**).

of recycling endosomes in growth cone dynamics. In addition, it could be used to control cellular processes such as polarization, signalling and outgrowth by depleting or accumulating cargo at specific sites. For example, increased axonal targeting of certain cargoes might promote axon regeneration after injury and provide novel insights into the mechanisms contributing to regeneration failure or success, both in culture and in different animal models[28].

Online Content Methods, along with any additional Extended Data display items and Source Data, are available in the online version of the paper; references unique to these sections appear only in the online paper.

Received 15 May; accepted 1 December 2014.
Published online 7 January 2015.

1. Vale, R. D. The molecular motor toolbox for intracellular transport. *Cell* **112,** 467–480 (2003).
2. Sheng, Z. H. & Cai, Q. Mitochondrial transport in neurons: impact on synaptic homeostasis and neurodegeneration. *Nature Rev. Neurosci.* **13,** 77–93 (2012).
3. Korolchuk, V. I. *et al.* Lysosomal positioning coordinates cellular nutrient responses. *Nature Cell Biol.* **13,** 453–460 (2011).
4. Yadav, S. & Linstedt, A. D. Golgi positioning. *Cold Spring Harb. Perspect. Biol.* http://dx.doi.org/10.1101/cshperspect.a005322 (2011).
5. Sadowski, L., Pilecka, I. & Miaczynska, M. Signaling from endosomes: location makes a difference. *Exp. Cell Res.* **315,** 1601–1609 (2009).
6. Ori-McKenney, K. M., Jan, L. Y. & Jan, Y. N. Golgi outposts shape dendrite morphology by functioning as sites of acentrosomal microtubule nucleation in neurons. *Neuron* **76,** 921–930 (2012).
7. Spillane, M., Ketschek, A., Merianda, T. T., Twiss, J. L. & Gallo, G. Mitochondria coordinate sites of axon branching through localized intra-axonal protein synthesis. *Cell Rep.* **5,** 1564–1575 (2013).
8. Courchet, J. *et al.* Terminal axon branching is regulated by the LKB1-NUAK1 kinase pathway via presynaptic mitochondrial capture. *Cell* **153,** 1510–1525 (2013).
9. Golachowska, M. R., Hoekstra, D. & van IJzendoorn, S. C. Recycling endosomes in apical plasma membrane domain formation and epithelial cell polarity. *Trends Cell Biol.* **20,** 618–626 (2010).
10. Higuchi, Y., Ashwin, P., Roger, Y. & Steinberg, G. Early endosome motility spatially organizes polysome distribution. *J. Cell Biol.* **204,** 343–357 (2014).
11. Eva, R. *et al.* ARF6 directs axon transport and traffic of integrins and regulates axon growth in adult DRG neurons. *J. Neurosci.* **32,** 10352–10364 (2012).
12. Eva, R. *et al.* Rab11 and its effector Rab coupling protein contribute to the trafficking of β1 integrins during axon growth in adult dorsal root ganglion neurons and PC12 cells. *J. Neurosci.* **30,** 11654–11669 (2010).
13. Kennedy, M. J. *et al.* Rapid blue-light-mediated induction of protein interactions in living cells. *Nature Methods* **7,** 973–975 (2010).
14. Strickland, D. *et al.* TULIPs: tunable, light-controlled interacting protein tags for cell biology. *Nature Methods* **9,** 379–384 (2012).
15. Kapitein, L. C. *et al.* Probing intracellular motor protein activity using an inducible cargo trafficking assay. *Biophys. J.* **99,** 2143–2152 (2010).
16. Kapitein, L. C. *et al.* Myosin-V opposes microtubule-based cargo transport and drives directional motility on cortical actin. *Curr. Biol.* **23,** 828–834 (2013).
17. Correia, S. S. *et al.* Motor protein-dependent transport of AMPA receptors into spines during long-term potentiation. *Nature Neurosci.* **11,** 457–466 (2008).
18. Wagner, W., Brenowitz, S. D. & Hammer, J. A. III. Myosin-Va transports the endoplasmic reticulum into the dendritic spines of Purkinje neurons. *Nature Cell Biol.* **13,** 40–48 (2011).
19. Wang, Z. *et al.* Myosin Vb mobilizes recycling endosomes and AMPA receptors for postsynaptic plasticity. *Cell* **135,** 535–548 (2008).
20. Hammer, J. A. III & Wagner, W. Functions of class V myosins in neurons. *J. Biol. Chem.* **288,** 28428–28434 (2013).
21. Bhuin, T. & Roy, J. K. Rab11 is required for embryonic nervous system development in *Drosophila*. *Cell Tissue Res.* **335,** 349–356 (2009).
22. Encalada, S. E. & Goldstein, L. S. Biophysical challenges to axonal transport: motor-cargo deficiencies and neurodegeneration. *Ann. Rev. Biophy.* **43,** 141–169 (2014).
23. Sheng, Z. H. Mitochondrial trafficking and anchoring in neurons: new insight and implications. *J. Cell Biol.* **204,** 1087–1098 (2014).
24. Sun, T., Qiao, H., Pan, P. Y., Chen, Y. & Sheng, Z. H. Motile axonal mitochondria contribute to the variability of presynaptic strength. *Cell Rep.* **4,** 413–419 (2013).
25. Chen, Y. & Sheng, Z. H. Kinesin-1-syntaphilin coupling mediates activity-dependent regulation of axonal mitochondrial transport. *J. Cell Biol.* **202,** 351–364 (2013).
26. Kang, J. S. *et al.* Docking of axonal mitochondria by syntaphilin controls their mobility and affects short-term facilitation. *Cell* **132,** 137–148 (2008).
27. Niopek, D. *et al.* Engineering light-inducible nuclear localization signals for precise spatiotemporal control of protein dynamics in living cells. *Nat. Commun.* **5,** 4404 (2014).
28. Bradke, F., Fawcett, J. W. & Spira, M. E. Assembly of a new growth cone after axotomy: the precursor to axon regeneration. *Nature Rev. Neurosci.* **13,** 183–193 (2012).

Supplementary Information is available in the online version of the paper.

Acknowledgements We are grateful to C. Tucker, T. Inoue, Z.-H. Sheng, G. Banker, R. Prekeris, P. Schätzle and M. Esteves da Silva for sharing reagents and to C. Wierenga and A. Akhmanova for discussions. This research is supported by the Dutch Technology Foundation STW and the Foundation for Fundamental Research on Matter (FOM), which are part of the Netherlands Organisation for Scientific Research (NWO). Additional support came from NWO (NWO-ALW-VICI to C.C.H and NWO-ALW-VIDI to L.C.K.) and the European Research Council (ERC starting grant to L.C.K.).

Author Contributions L.C.K. and C.C.H. initiated research. P.B. created reagents. P.B., M.A., C.C.H. and L.C.K. designed experiments. P.B. and M.A. performed experiments. P.B., M.A. and L.C.K. analysed data. P.B., M.A., C.C.H. and L.C.K. wrote the manuscript.

Author Information Reprints and permissions information is available at www.nature.com/reprints. The authors declare no competing financial interests. Readers are welcome to comment on the online version of the paper. Correspondence and requests for materials should be addressed to C.C.H. (c.hoogenraad@uu.nl) and L.C.K. (l.kapitein@uu.nl).

METHODS

DNA constructs. The following constructs have been described: tagRFPt[29] (gift from R. Tsien), pCIBN(deltaNLS)-pmGFP and pCry2PHR-mCherryN1 (ref. 13; addgene, plasmids 26867 and 26866), mid(SS/TM)-GFP-LOVpep and ePDZb1-mCherry[14] (addgene, plasmids 34972 and 34981), TOM20-mCherry-GAI[30] (gift from T. Inoue), HA-rab11a (ref. 31), Kif1a(1–489)-GFP-FRB, Kif5b(1–807)-GFP-FRB, MyoVb(1–1090)-GFP-FRB, HA-BicD2(1–594)-FRB and Pex3(1–42)-mRFP[15], pGW2-pex26 and pGW2-Kif17-GFP-pex26 (ref. 16), GFP-SNPH[26] (gift from Z. Sheng), GFP-RCP[32] (RAB11FIP1, gift from R. Prekeris), NPY-GFP[33] and GFP-MACF18 (ref. 34).

Cloning vectors and fluorescent tags. The constructs used in this study were cloned in the mammalian expression vectors pGW1-CMV, pGW2-CMV and/or pβactin[15]. pβactin-GFP, pβactin-tagRFPt, pβactin-tagBFP and pβactin-iRFP were generated by ligating the fluorescent proteins in the SalI and SpeI site of pβactin.

Tagging motor proteins, adaptors and anchors with CIBN and ePDZb1. To generate myoVb(1–1090)-GFP-CIBN and myoVb(1–1090)-GFP-ePDZb1, amino acids 1–1090 of myosin-Vb were cloned in the AscI and EcoRI sites of pβactin-GFP, and either CIBN or ePDZb1 was inserted downstream of GFP using a PCR-based strategy. Similarly, myoVb-iRFP-CIBN was made using the pβactin-iRFP vector backbone. Kif1a(1–383)-GFP-CIBN and Kif1a(1–383)-GFP-ePDZb1 were generated by ligating amino acids 1–383 of mouse KIF1A in the AscI and SalI sites of pβactin-GFP. Subsequently, PCR-amplified CIBN or ePDZb1 was inserted downstream of GFP. Haemagglutinin (HA)-tagged HA-BicD2(1–500)-CIBN and BicD2(1–500)-ePDZb1 were cloned by inserting PCR-amplified BicD2(1–500) (refered to as BICDN in the main text) into the pβactin vector backbone. Subsequently, CIBN and ePDZb1were ligated downstream of BicDN. Kif5b(1–807)-GFP-ePDZb1 was made by inserting PCR-amplified Kif5b(1–807) into the AscI and BamHI sites of a GFP-ePDZb1 backbone. To create SNPH(45–748)-GFP-ePDZb1, PCR-amplified *SNPH* (forward primer: 5′-AGCGCTAAGCTTGCCACCATGGCCATGTCCCTGCAGGGAAG-3′ and reverse primer: 5′-GCCCTTGCTCACCATAGTCGACCCCACTACCACAGCCAGCAGATCCAC-3′) was inserted into a GFP-ePDZb1 backbone using Cold Fusion cloning (System Biosciences).

Tagging peroxisomes, RAB11 vesicles and mitochondria with LOVpep and Cry2PHR. To generate Pex3-mRFP-LOVpep (PEX–LOV), LOVpep, including a 9-amino-acid linker (GGSGGSGGS), was ligated in the AscI and SalI sites of pGW1-pex3-mRFP. To make TOM20-mCherry-LOVpep, Pex3-mRFP was replaced by TOM20(1–34)-mCherry using the HindIII and AscI sites. To create Cry2PHR-tagRFPt-Rab11 and FKBP-tagRFPt-Rab11, Rab11a was introduced in the SpeI and NotI sites of pβactin-tagRFPt. Subsequently, PCR-amplified FKBP or Cry2PHR was ligated upstream of tagRFPt. FRB-tagBFP-LOVpep was made by inserting LOVpep, including a 9-amino-acid linker, in the SpeI and NotI sites of pβactin-tagBFP. Subsequently, PCR -amplified FRB was cloned upstream of tagBFP.

Other constructs. pJPA5-TfR-GFP (a gift from G. Banker) was cloned into a β-actin vector. Membrane targeting of GFP was achieved by inserting the 40 most N-terminal residues of the MARCKS protein with an additional palmitoylation site at residue 3 (ref. 35) into GW2-tagRFPt. To generate mRFP-actin, human cytoplasmic β-actin was cloned from pEGFP-actin (Clontech) in the β-actin-mRFP vector.

Cell cultures and transfection. COS-7 cells were cultured in DMEM/Ham's F10 (1:1) medium containing 10% FCS and penicillin/streptomycin. Then, 2–4 days before transfection, cells were plated on 24-mm diameter coverslips. Cells were transfected with Fugene6 transfection reagent (Roche) according to the manufacturer's protocol and imaged one day after transfection.

Primary hippocampal cultures were prepared from embryonic day 18 (E18) rat brains[36]. Cells were plated on coverslips coated with poly-L-lysine (30 mg ml^{-1}) and laminin (2 mg ml^{-1}) at a density of 75,000 per well. Hippocampal cultures were grown in Neurobasal medium (NB) supplemented with B27, 0.5 mM glutamine, 12.5 mM glutamate, and penicillin plus streptomycin. Hippocampal neurons were transfected 48 h before imaging with lipofectamine 2000 (Invitrogen). DNA (3.6 μg per well) was mixed with 6.6 μl lipofectamine 2000 in 400 ml NB, incubated for 30 min, and then added to the neurons in NB supplemented with 0.5 mM glutamine at 37 °C in 5% CO_2 for 60 min. Next, neurons were washed with NB and transferred to the original medium at 37 °C in 5% CO_2 for 2 days. Transport assays targeting dendritic spines were imaged at day-*in-vitro* (DIV) 20–22 and growth cone or mitochondria assays were imaged at DIV 3–7.

Live-cell image acquisition. Time-lapse live-cell imaging of COS-7 cells and hippocampal neurons was performed on a Nikon Eclipse TE2000E (Nikon) equipped with an incubation chamber (Tokai Hit; INUG2-ZILCS-H2) mounted on a motorized stage (Prior)[16]. Coverslips (24 mm) were mounted in metal rings, immersed in 0.6 ml Ringer's solution (10 mM HEPES, 155 mM NaCl, 5 mM KCl, 1 mM $CaCl_2$, 1 mM $MgCl_2$, 2 mM NaH_2PO_4 and 10 mM glucose, pH 7.4) or full medium (RAB11 imaging in COS-7 cells) or conditioned medium (Neuron imaging), and maintained at 37 °C and 5% CO_2. Cells were imaged every 5, 10 or 30 s for 5–50 min using a 40× objective (Plan Fluor, numerical aperture (NA) 1.3, Nikon) and a Coolsnap HQ2 CCD camera (Photometrics). Dense-core vesicles were imaged using a 100× objective (Apo TIRF, 1.49 NA, Nikon) on a Evolve 512 EMCCD camera (Photometrics). A mercury lamp (Osram) and filter wheel containing ET-GFP (49002), ET-dsRed (49005), ET-mCherry (49008) and ET-GFPmCherry (59022) emission filters (all Chroma) were used for excitation and for global activation. For global activation, the GFP excitation filter was used to illuminate the sample for 100–150 ms with every image acquisition during the periods of blue-light exposure. In most experiments, the activation intensity was around 10 W cm^{-2} and the total irradiance was about 30 times higher than the minimum irradiance required for full activation (see Extended Data Fig. 4h). These settings allowed us to monitor the dynamics of GFP-labelled proteins or growth cones during activation.

For local illumination of specific areas using a 488-nm laser line, a FRAP scanning head was used (FRAP L5 D-CURIE, Curie Institute). Compared to standard FRAP experiments the laser was used at much lower intensities.

Live-cell spinning disk confocal microscopy of growth cones and spines of hippocampal neurons was performed on a Nikon Eclipse-Ti (Nikon) microscope with a Plan Apo VC, 60×, 1.40 NA oil objective (Nikon). The microscope is equipped with a motorized stage (ASI; PZ-2000), a Perfect Focus System (Nikon), an incubation chamber (Tokai Hit; INUG2-ZILCS-H2) and uses MetaMorph 7.7.11 software (Molecular Devices) to control the camera and all motorized parts. Confocal excitation and detection is achieved using 100 mW Vortran Stradus 405 nm, 100 mW Cobolt Calypso 491 nm and 100 mW Cobolt Jive 561nm lasers and a Yokogawa spinning disk confocal scanning unit (CSU-X1-A1N-E; Roper Scientific) equipped with a triple-band dichroic mirror (z405/488/568trans-pc; Chroma) and a filter wheel (CSUX1-FW-06P-01; Roper Scientific) containing 4′,6-diamidino-2-phenylindole (DAPI; ET-DAPI (49000)), GFP (ET-GFP (49002)) and mCherry (ET-mCherry (49008)) emission filter (all Chroma). Confocal images were acquired with a QuantEM:512 SC EMCCD camera (Photometrics) at a final magnification of 110 nm per pixel, including the additional 2.5× magnification introduced by an additional lens mounted between scanning unit and camera (VM Lens C-2.5X; Nikon). Local activation of photo-heterodimerization was achieved with an ILas FRAP system (Roper Scientific France/ PICT-IBiSA, Institut Curie) and 491 nm laser line at low power. To couple FRB-LOV to FKBP-RAB11, rapalog (AP21967, ARIAD) was dissolved to 0.1 mM in ethanol. Then 20 min before imaging, 0.2 ml of culture medium with rapalog (400 nM) was added to establish a final rapalog concentration of 100 nM.

Image processing and analysis. Images of live cells were processed and analysed using MetaMorph (Molecular Devices), LabVIEW (National Instruments) software and ImageJ (NIH). If not followed by a quantification in a subsequent panel, representative images are representative of 60–90% of the cells studied in the same conditions, with at least five responding cells per condition (except for Extended Data Fig. 4f with three responding cells, because we used the system in Extended Data Fig. 4i, j for all subsequent experiments). The exact organelle distributions and dynamics mostly depended on the levels of protein overexpression, which could not be examined before the experiment without triggering heterodimerization. For example, if the motor were poorly expressed, less redistribution was observed. This was most apparent in experiments where three or more constructs were co-expressed, some of which without fluorescent marker that could be used to confirm expression of the motor.

Quantification of redistribution dynamics. Before analysis, cells were masked to exclude contributions from neighbouring cells to the analysis. For the colour-coded redistribution plots, all images of a time-lapse recording were thresholded at ~5–20 times the standard deviation of the background above the background to yield binary images that were subsequently overlaid non-transparently starting with the final frame (first frame on top) in Fig. 1d, and starting with the first frame (last frame on top) in Fig. 3c. Each frame was coloured using a time-coded gradient that ran from orange to white before and from white to green after blue-light illumination. To quantify the radial redistribution of peroxisomes upon recruitment of (additional) motor proteins, the radius required to include 90% of the total intensity of the cell, $R_{90\%}(t)$, was calculated for each frame as described previously[15].

To quantify changes in the dynamics of peroxisomes or RAB11 vesicles upon recruitment of (additional) motor proteins, we calculated the time-dependent frame-to-frame correlation index $c_\tau(t)$[16] by first calculating the integrated intensity of the image obtained by multiplying the frames acquired at t and $t+\Delta t$, that is, $\sum_{x=1}^{X}\sum_{y=1}^{Y} i(x,y,t)i(x,y,t+\Delta t)$, in which $i(x, y, t)$ is the intensity at pixel (x, y) of the frame acquired at time t. These values can then be normalized using either the integrated intensity of the image acquired at t or $t+\Delta t$, that is, $\sum_{x=1}^{X}\sum_{y=1}^{Y} i^2(x,y,t)$ or $\sum_{x=1}^{X}\sum_{y=1}^{Y} i^2(x,y,t+\Delta t)$. For our analyis, we used the average result of these two normalizations as our readout, that is,

$$c_\tau(t) = \frac{1}{2}\left(\frac{\sum_{x=1}^{X}\sum_{y=1}^{Y} i(x,y,t)i(x,y,t+\tau)}{\sum_{x=1}^{X}\sum_{y=1}^{Y} i^2(x,y,t)} + \frac{\sum_{x=1}^{X}\sum_{y=1}^{Y} i(x,y,t)i(x,y,t+\tau)}{\sum_{x=1}^{X}\sum_{y=1}^{Y} i^2(x,y,t+\tau)}\right).$$

$c_\tau(t)$ will be 1 if the particles are completely anchored and their positions unchanged after a time τ, whereas $c_\tau(t)$ will be 0 if all particles moved to previously unoccupied locations. In practice, $c_\tau(t)$ will remain finite even in very dynamic samples, because a subset of particles will move to locations that were occupied by different particles in the first image. In all our analyses, we used frame-to-frame differences. For analysing the correlation index in small regions (Figs 2d and Extended Data Fig. 4l), measurements were averaged over six adjacent time points.

To determine local changes in fluorescence intensities over time (Fig. 1i–l), the mean grey value of the first-frame-subtracted recording (Fig. 1l), or last-frame-subtracted recording (Fig. 1k) was measured, and the maximum was set to 1. Individual peroxisomes or RAB11 vesicle trajectories were obtained using the MTrackJ plugin in ImageJ[37].

Analysis of spine entries. Peroxisomes and RAB11 vesicles were imaged at 1-s intervals, preferably in two dendrites of the same neuron, of which one was illuminated with pulses of 491 nm light directly before the frames indicated. Spine entries during periods of 100 s before, 100 s during and 200 s after illumination were detected manually using the Cell Counter plugin in ImageJ to determine the fraction of cargo-targeted spines and the frame of spine entry. The mean percentage of spines targeted with peroxisomes was compared with a Mann–Whitney test (Fig. 2i), and the mean percentages of peroxisome and endosome entries were subjected to a Kruskal–Wallis ANOVA with Dunn's post-hoc test (Fig. 2j) or a one-way ANOVA with Bonferroni's post-hoc test (Extended Data Fig. 4p), respectively. The half-time of peroxisome entries into dendritic spines after illumination was estimated by fitting a single exponential function ($R^2 = 0.9942$) through the inverted cumulative histogram of the observed entry events after 491 nm illumination was stopped.

Analysis of axon growth and growth cone area. Axonal growth was manually tracked using the MTrackJ plugin in ImageJ[37]. The percentages of growth cones exhibiting light-induced reduction in dynamics or growth enhancements were compared using unpaired two-tailed *t*-tests (Fig. 3g, h). In all our experiments, only the RFP channel was available for imaging without triggering photo-heterodimerization before, during and after exposure to blue light. We used this channel to image FKBP-tagRFPt-RAB11 to verify that light-controlled recruitment of BICDN induced the removal of RAB11 endosomes (Extended Data Fig. 8a, b). FKBP-RAB11 was enriched at vesicles-like structures, whose dynamics altered upon light-dependent recruitment of BICDN to recruit dynein. In addition, FKBP-RAB11 diffusely filled the axon, which could be used to determine axon morphology and size with precision comparable to a cytoplasmic GFP fill (Extended Data Fig. 8c). We counted the positive pixels in a binarized image obtained by thresholding the median-filtered tagRFPt image, followed by two erosions and closure[38]. Because tag-RFPt fluorescence of this construct showed a threefold increase in intensity upon 491 nm excitation (see Extended Data Fig. 8a), we established a dynamic threshold T that scaled with the maximum intensity of the object, that is, $T = I_{bg} + \sigma_{bg} + 0.02(I_{max})$, in which I_{bg} and σ_{bg} are the average and standard deviation of the intensity in an area outside the axon, respectively, and I_{max} is the average of the top 2% intensity values above $I_{bg} + \sigma_{bg}$. Using these parameters, changes in area are independent of the changes in intensity upon exposure to blue light or due to dynein-mediated removal of RAB11 vesicles (see Extended Data Fig. 8d, e).

Relative decreases in growth cone RAB11-FKBP signal were calculated by rescaling all intensity values normalized initially to $t_{-2:30\,\mathrm{min}}$ to the average intensity value of –FRB–LOV control growth cones at $t_{8\,\mathrm{min}}$ (see Extended Data Fig. 8a). To calculate changes in growth cone area before blue-light illumination, we compared single growth cone area values averaged over three frames at $t_{0\,\mathrm{min}}$ and $t_{-4\,\mathrm{min}}$ relative to illumination onset (See Extended Data Fig. 8g, h). Analogously, comparing values at $t_{8\,\mathrm{min}}$ and $t_{0\,\mathrm{min}}$ shows net growth during blue-light illumination (see Extended Data Fig. 8i, j). All of these results were compared using Mann–Whitney tests (Extended Data Fig. 8b, g, i). All statistical testing was performed in GraphPad Prism 5 software. No statistical method was used to predetermine sample size.

Immunofluorescence cell staining, imaging and antibodies. COS-7 cells (1 day after transfection) or primary hippocampal neurons (2 days after transfection) were either kept in the dark or illuminated for 10 min using a blue light-emitting diode mounted in the incubator. Afterwards, cells were fixed at room temperature for 10 min with 4% paraformaldehyde (PFA), 4% sucrose. For detection of EB1, cells were fixed for 5 min at −20 °C in 100% ice-cold methanol supplemented with 1 mM EGTA, followed by 5 min post-fixation at room temperature in 4% PFA, 4% sucrose. After fixation, cells were washed three times in PBS and incubated overnight at 4 °C in GDB buffer (0.1% BSA, 450 mM NaCl, 0.3% Triton X-100 and 16.7 mM phosphate buffer, pH 7.4) containing the primary antibody. The next day, cells were washed three times for 10 min with PBS, followed by a 1-h incubation at room temperature with the secondary antibody in GDB buffer. After washing cells three times for 10 min in PBS, slides were mounted in Vectashield mounting medium (Vector Laboratories). Images were taken with a Nikon eclipse 80i upright fluorescence microscope and a Coolsnap HQ2 CCD camera (Photometrics), using a 40× oil objective (Plan Fluor, NA 1.3), 60× oil objective (Plan Apo VC, NA 1.4) or 100× oil objective (Plan Apo VC, NA 1.4).

Antibodies and reagents used: mouse anti-Cytochrome *c* (6H2.B4, 556432, BD Biosciences), mouse anti-PDI (RL90, MA3-019, Affinity BioReagents), phalloidin-Alexa647 (A22287, Invitrogen), mouse anti-alpha tubulin (B-5-1-2, T-5168, Sigma), mouse anti-EB1 (610535, BD Transduction), mouse anti-Lamp1 (this antibody developed by J. T. August and J .E. K. Hildreth, was obtained from the hybridoma bank, created by the NICHD of the NIH and maintained at The University of Iowa, Department of Biology), mouse anti-EEA1 (BD Transduction), rabbit anti-RAB11 (71-5300, Invitrogen), rabbit anti-Homer-1 (160-002, SySy), Alexa 488-, Alexa 568-, Alexa 647-conjugated secondary antibodies (Invitrogen).

GFP pull-down and western blotting. HEK cells were cultured in DMEM/Ham's F10 (1:1) medium containing 10% FCS and penicillin/streptomycin. Then 1 day after plating, HEK293T cells were transfected using polyethylenimine (PEI; Polysciences). After 24 h, GFP beads (GFP-Trap_M, Chromotek) were washed in washing buffer (TBS, 0.5% Triton X-100 and protease inhibitor) and incubated for 1 h in blocking buffer (TBS, 0.5% Triton X-100, 2% glycerol, 2% chicken egg white). Meanwhile, cells were collected in ice-cold TBS, pelleted and lysed in extraction buffer (TBS 0.5% Triton X-100, protease inhibitor, phosphatase inhibitor (Roche), 100 μM GTPγS, 5 mM $MgCl_2$, pH 8.0). Cell lysates were centrifuged for 15 min at 4 °C at12,000*g*, followed by a 1.5-h incubation of the supernatants with the washed GFP beads, while rotating at 4 °C. Beads were collected using a magnetic separator and washed four times. Samples were eluted in SDS sample buffer, boiled for 5 min and loaded onto SDS–PAGE gels and blotted on PVDF membranes (Millipore). Blots were blocked in 5% milk in PBST (0.1% Tween in PBS) and incubated overnight at 4 °C (primary antibody) or for 1 h at room temperature (secondary antibody conjugated to horseradish peroxidase) in PBST. Finally, blots were developed using enhanced chemiluminescent western blotting substrate (Pierce).

Antibodies used: rabbit anti-TagRFPt (ab234, Evrogen), rabbit anti-GFP (ab290, abcam) and anti-rabbit IgG antibody conjugated to horseradish peroxidase (DAKO).

29. Shaner, N. C. *et al.* Improving the photostability of bright monomeric orange and red fluorescent proteins. *Nature Methods* **5,** 545–551 (2008).
30. Miyamoto, T. *et al.* Rapid and orthogonal logic gating with a gibberellin-induced dimerization system. *Nature Chem. Biol.* **8,** 465–470 (2012).
31. Hoogenraad, C. C. *et al.* Neuron specific Rab4 effector GRASP-1 coordinates membrane specialization and maturation of recycling endosomes. *PLoS Biol.* **8,** e1000283 (2010).
32. Peden, A. A. *et al.* The RCP-Rab11 complex regulates endocytic protein sorting. *Mol. Biol. Cell* **15,** 3530–3541 (2004).
33. Schlager, M. A. *et al.* Pericentrosomal targeting of Rab6 secretory vesicles by Bicaudal-D-related protein 1 (BICDR-1) regulates neuritogenesis. *EMBO J.* **29,** 1637–1651 (2010).
34. Honnappa, S. *et al.* An EB1-binding motif acts as a microtubule tip localization signal. *Cell* **138,** 366–376 (2009).
35. De Paola, V., Arber, S. & Caroni, P. AMPA receptors regulate dynamic equilibrium of presynaptic terminals in mature hippocampal networks. *Nature Neurosci.* **6,** 491–500 (2003).
36. Kapitein, L. C., Yau, K. W. & Hoogenraad, C. C. Microtubule dynamics in dendritic spines. *Methods Cell Biol.* **97,** 111–132 (2010).
37. Meijering, E., Dzyubachyk, O. & Smal, I. Methods for cell and particle tracking. *Methods Enzymol.* **504,** 183–200 (2012).
38. Russ, J. C. *The Image Processing Handbook* 5th edn (CRC/Taylor and Francis, 2007).

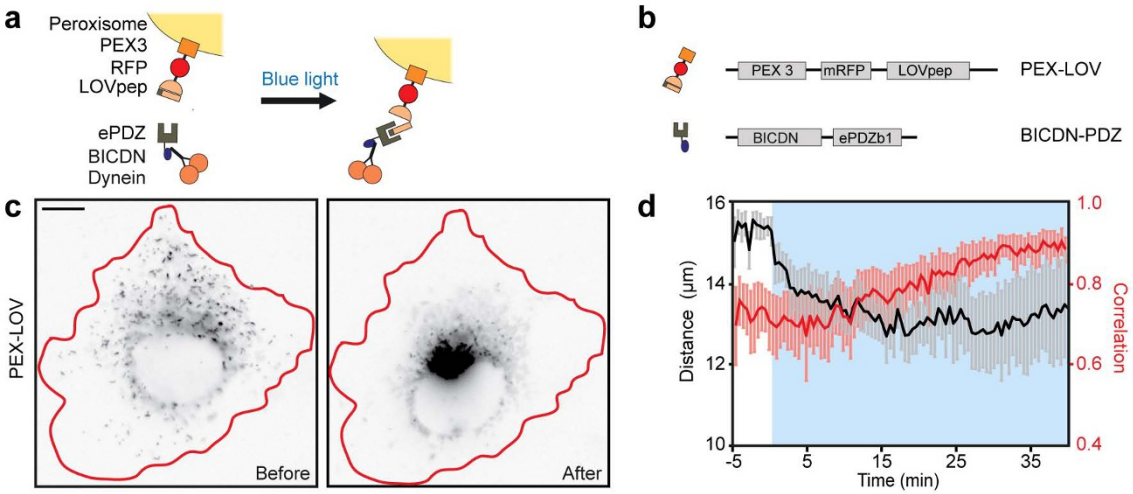

Extended Data Figure 1 | Optical control of dynein-based cargo motility. **a**, **b**, Assay and constructs. A fusion construct of PEX3, monomeric red fluorescent protein (mRFP) and LOVpep (PEX–LOV) targets peroxisomes. After blue-light illumination, a fusion of the N terminus of the dynein adaptor BICD2 and ePDZb1 (BICDN–PDZ) is recruited to peroxisomes. **c**, Peroxisome distribution in a COS-7 cell expressing PEX–LOV and BICDN–PDZ before and during light-induced recruitment of dynein (inverted contrast). Red lines indicate cell outline. Scale bar, 10 μm. See Supplementary Video 1. **d**, Black: time trace of $R_{90\%}$ (radius of circle enclosing 90% of cellular fluorescence; see Methods) in cells expressing PEX–LOV and BICDN–PDZ ($n = 5$ cells). Red: correlation index (frame-to-frame differences in the peroxisome recordings; see Methods) of the same cells. Blue-light illumination is indicated in blue; mean ± s.e.m.

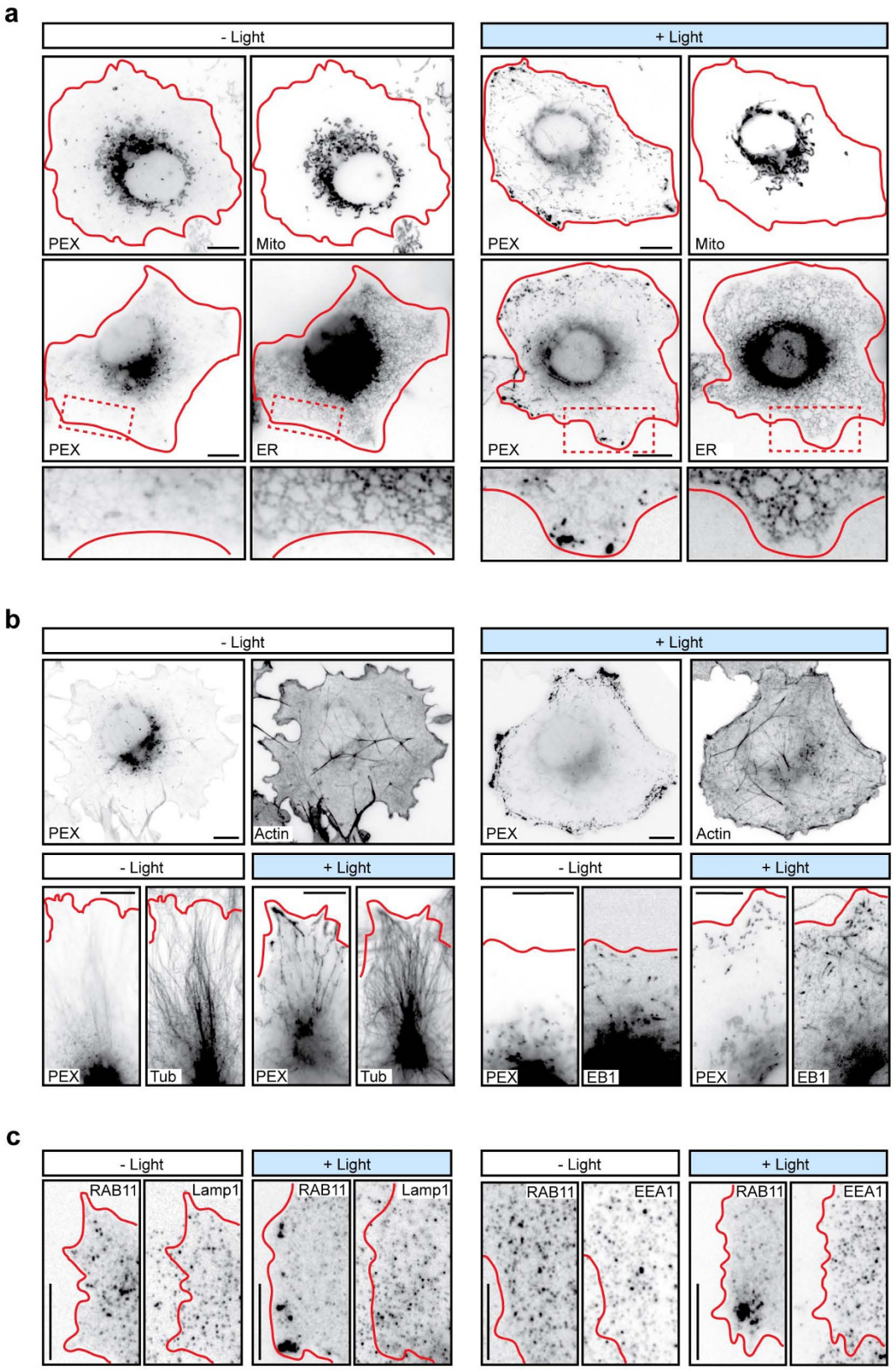

Extended Data Figure 2 | Light-induced organelle redistribution is organelle-specific and does not affect the cytoskeleton. **a**, Images of fixed cells expressing PEX–LOV and KIF–PDZ, showing the distribution of peroxisomes and mitochondria (anti-cytochrome-c), or peroxisomes and the endoplasmic reticulum (anti-protein disulfide isomerase (PDI)) in the absence (left) or presence (right) of blue light. **b**, Images of fixed cells expressing PEX–LOV and KIF–PDZ, showing the distribution of peroxisomes and phalloidin, α-tubulin or EB1 staining in the absence or presence of blue light. **c**, Images of fixed cells expressing FKBP–RAB11, FRB–LOV and KIF–PDZ, showing the distribution of RAB11 recycling endosomes together with lysosomes (anti-Lamp1) or early endosomes (anti-EEA1) in the absence or presence of blue light. Red lines indicate cell outline. Scale bars, 10 μm.

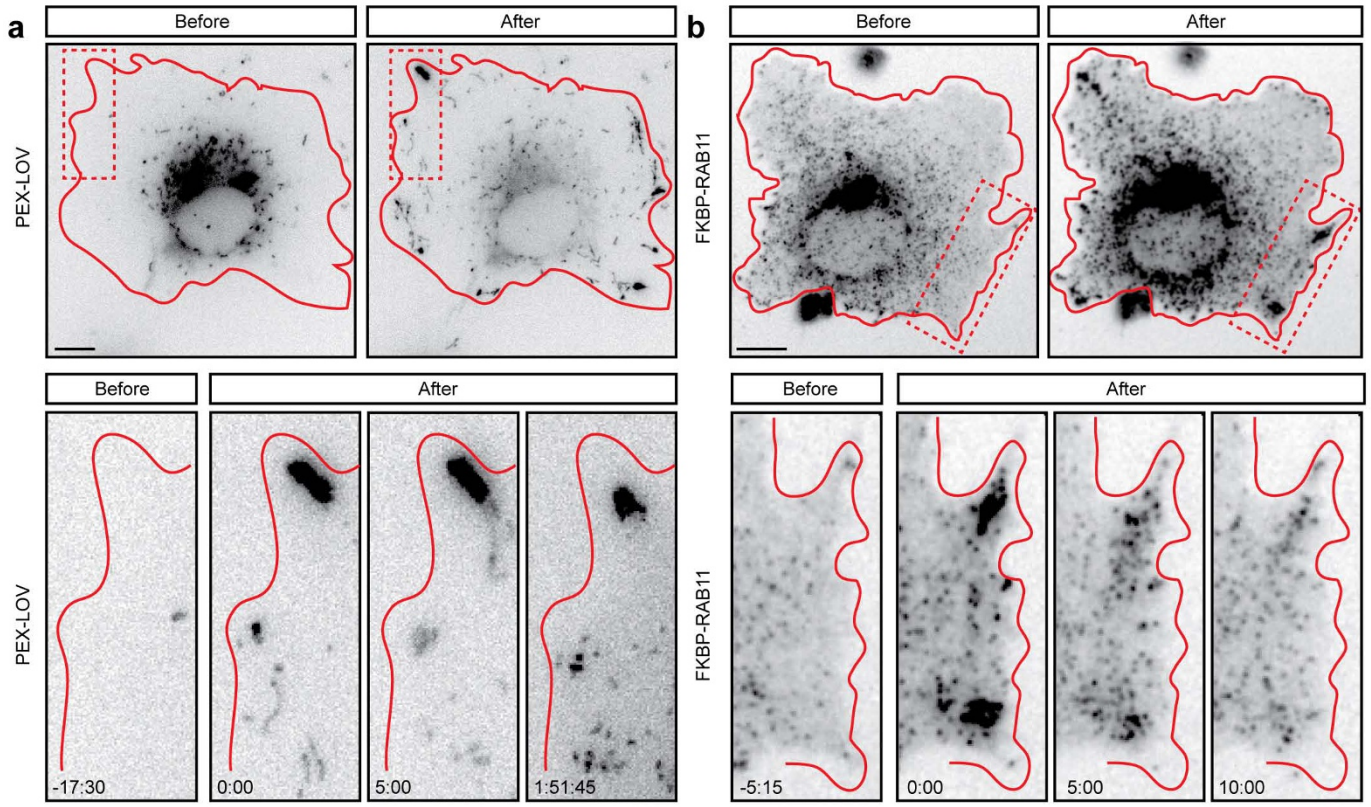

Extended Data Figure 3 | After light induced organelle displacement, peroxisomes remain at their newly obtained position whereas the distribution of recycling endosomes quickly reverses back to normal. **a**, Peroxisome distribution before and after exposure to blue light in cells expressing PEX–LOV and KIF–PDZ. Blue-light illumination was terminated at $t_{0:00}$. **b**, Distribution of RAB11 recycling endosomes before and after exposure to blue light in cells expressing FKBP–RAB11, FRB–LOV and KIF–PDZ. Blue light was turned off at $t_{0:00}$. Red lines indicate cell outline. Scale bars, 10 µm. See Supplementary Video 4.

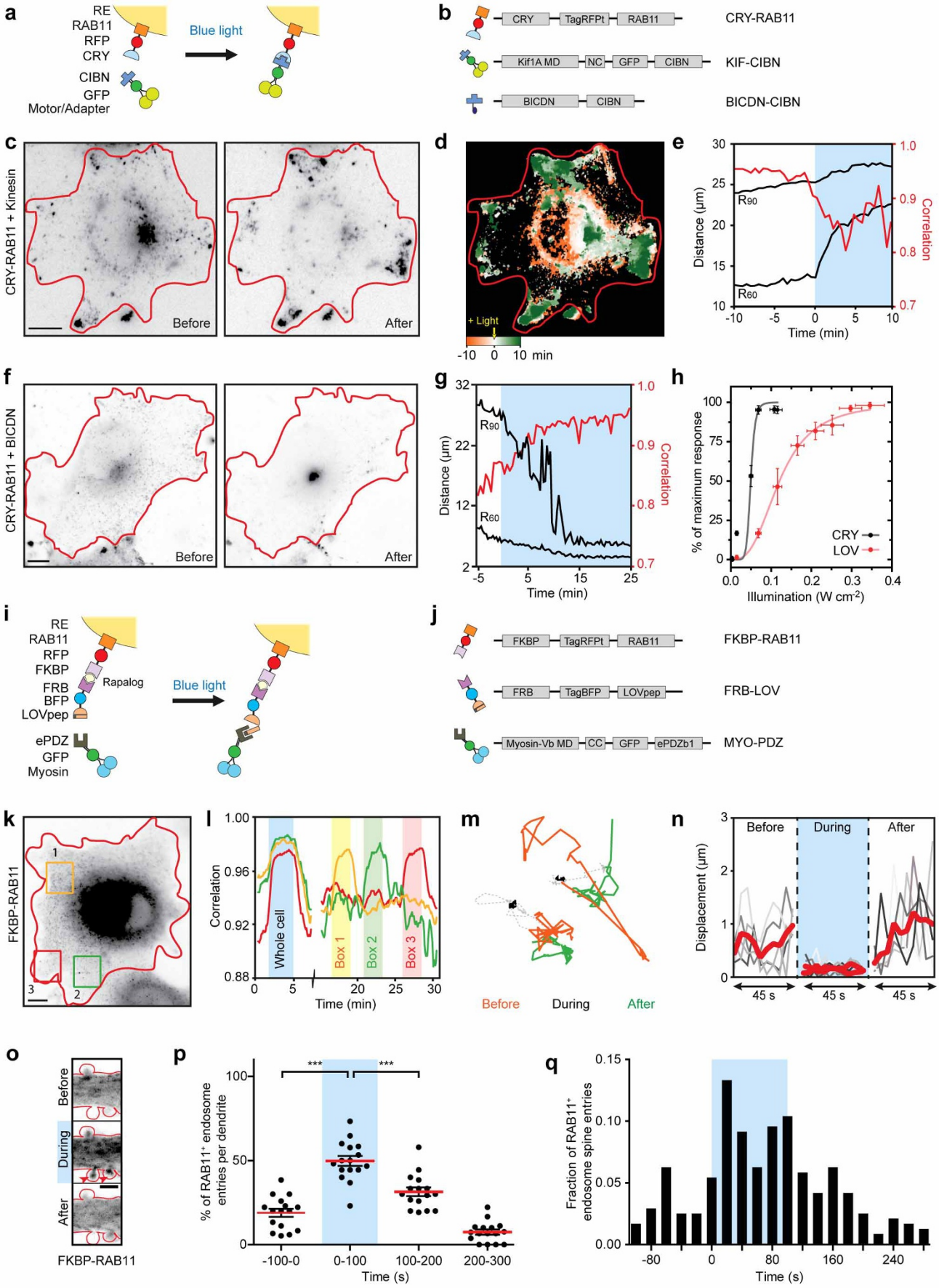

Extended Data Figure 4 | Spatiotemporal control of recycling endosome distribution and dynamics. **a**, **b**, Assay and constructs. A fusion construct of Cry2PHR, tagRFPt and RAB11, (CRY–RAB11) targets RAB11 recycling endosomes. After blue-light illumination, a fusion of truncated KIF1A, GFP and CIBN (KIF–CIBN) or a fusion of truncated BICDN, GFP and CIBN (BICDN–CIBN) is recruited to RAB11 recycling endosomes. **c**, RAB11 vesicle distribution before and after light-induced recruitment of KIF1A (inverted contrast). Red lines indicate cell outline. Scale bar, 10 µm. **d**, Overlay of sequential binarized images from the recording in **c**, colour-coded by time as indicated. Orange marks the initial distribution of RAB11 vesicles, whereas green marks regions targeted after exposure to blue light. **e**, Time trace of the $R_{60\%}$ and $R_{90\%}$ (black) and the correlation index (red) of the cell shown in **c** and **d**. Blue box marks blue-light illumination. **f**, RAB11 distribution in a cell expressing CRY–RAB11 and BICDN–CIBN before and after blue-light illumination (inverted contrast). Red lines indicate cell outline. Scale bar, 10 µm. **g**, Time trace of the $R_{60\%}$ and $R_{90\%}$ (black) and correlation index for the cell shown in **f**. **h**, Irradiance response curve for cells transfected with CRY–PEX and KIF–CIBN (red), or PEX–LOV plus KIF–PDZ (black). To exclude activation failure due to poorly expressed motors, the number of cells reacting at each concentration was divided by the number of cells responding to subsequent high irradiance ($\sim$1.3 W cm^{-2}). Three biological replicates. Cells per intensity (for increasing intensities): 28, 21, 22, 20, 24, 22 and 20 for CRY, 30, 28, 33, 31, 28, 33, 33, 32 and 26 for LOV. Error bars depict s.e.m.; three biological replicates. Solid line shows fit to $R = 100 \cdot I^n / \left(I_0^n + I^n\right)$, with R the response, I the illumination intensity, I_0 the intensity at which the response is 50%, and n the Hill coefficient. For CRY–PEX and PEX–LOV, I_0 is 0.05 and 0.12 W cm^{-2}, respectively. **i**, **j**, Assay and constructs. A fusion construct of FKBP, tagRFPt and RAB11 (FKBP–RAB11) targets RAB11 recycling endosomes. Rapalog addition couples FKBP to FRB, leading to recruitment of the FRB, tagBFP and LOVpep fusion protein (FRB–LOV). After blue-light illumination a fusion of truncated myosin-Vb, GFP and ePDZb1 (MYO–PDZ) is recruited to RAB11 vesicles. **k**, RAB11 distribution in a cell expressing FKBP–RAB11, FRB–LOV and MYO–PDZ before sequential blue-light illumination of the regions marked with numbered boxes (inverted contrast). Scale bar, 10 µm. See Supplementary Video 5. **l**, Time traces of the correlation index in the areas shown in **k**. Blue box marks whole-cell exposure to blue light, whereas colored boxes indicate local illumination. **m**, Example trajectories of two RAB11 recycling endosomes before, during and after recruitment of myosin-Vb, as indicated. Data was acquired with 1-s intervals. For each period 40 s are shown. **n**, Frame-to-frame displacements of RAB11 recycling endosomes before, during and after light-induced recruitment of myosin-Vb (5 s interval). Thick lines show the average of five tracks in shades of grey. **o**, FKBP–RAB11 distribution (inverted contrast) in a dendrite and dendritic spines before, during and after blue-light illumination. Images are maximum projections spanning 60 s. Red lines indicate cell outline, arrowheads mark spines targeted with recycling endosomes during blue-light illumination. Scale bar, 2 µm. **p**, Percentage of recycling endosome spine entry events per dendrite before, during and after illumination in bins of 100 s. Blue box indicates blue-light illuminated interval, $n = 16$ dendrites in three independent experiments. Red bar denotes mean ± s.e.m., $^{***}P < 0.0001$, one-way ANOVA, Bonferroni's post-hoc test. **q**, Histogram of fraction of all ($n = 237$) recycling endosome spine entries in bins of 20 s. Blue box indicates blue-light-illuminated interval.

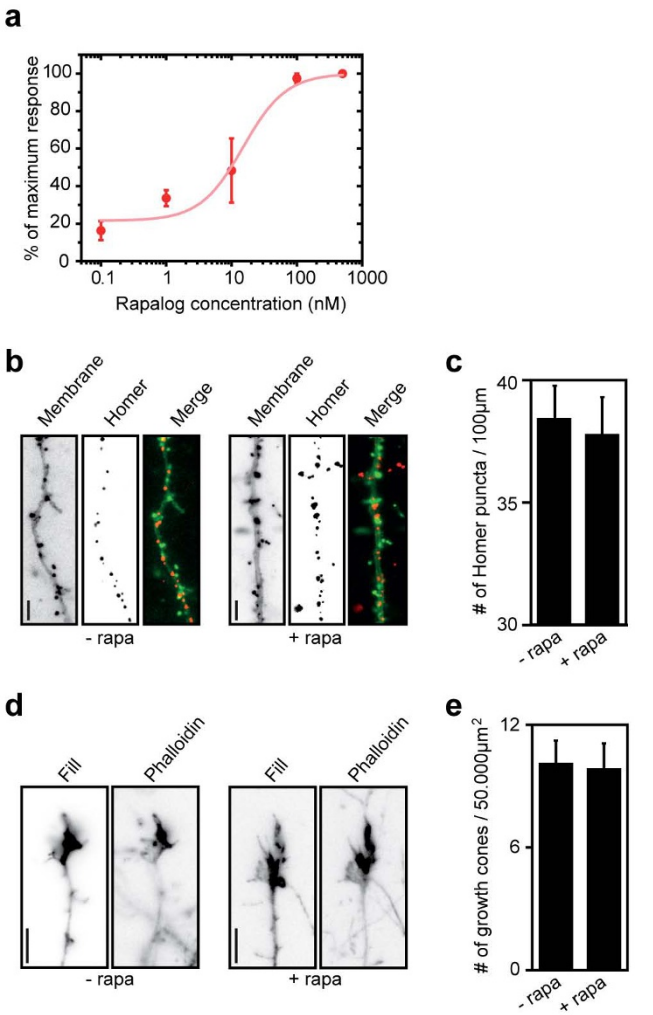

Extended Data Figure 5 | Rapalog in the nanomolar range is sufficient to recruit FRB–LOV to FKBP–RAB11 and does not affect the number of spines or growth cones in hippocampal neurons. **a**, Response curve of RAB11 recycling endosome relocalization in cells expressing FKBP–RAB11, FRB–LOV and KIF–PDZ exposed to blue light in relation to rapalog concentration. To exclude activation failure due to poorly expressed motors, the number of cells reacting at each concentration was divided by the number of cells responding to subsequent high rapalog concentration (1 µM). Solid line shows fit to $R = \left(R_{\min} I_0^n + 100 \cdot I^n\right) / \left(I_0^n + I^n\right)$, with R the response, c the rapalog concentration, c_0 the concentration at which the response is 50%, n the Hill coefficient, and $R_{\min}$ the response at 0 mM rapalog. $R_{\min}$ is 22% and c_0 is 15 nM. $n = 30$ (0.1 nM), 37 (1 nM), 30 (10 nM), 28 (100 nM) and 28 (500 nM) responsive cells from three independent experiments. Error bars depict s.e.m. **b**, Hippocampal neurons transfected with membrane–GFP incubated for 2.5 h in the presence or absence of 100 nM rapalog, co-stained with the post-synaptic marker Homer. **c**, Quantification of the number of Homer puncta per 100 µm dendrite length in the presence or absence of 100 nM rapalog ($n = 13$ neurons per condition). Error bars depict s.e.m. **d**, Hippocampal neurons transfected with GFP incubated for 2.5 h in the presence or absence of 100 nM rapalog, co-stained with phalloidin. **e**, Quantification of the number of growth cones per 50,000 µm^2 in the presence or absence of 100 nM rapalog, co-stained with phalloidin. $n = 19$. Scale bars, 5 µm. Error bars depict s.e.m.

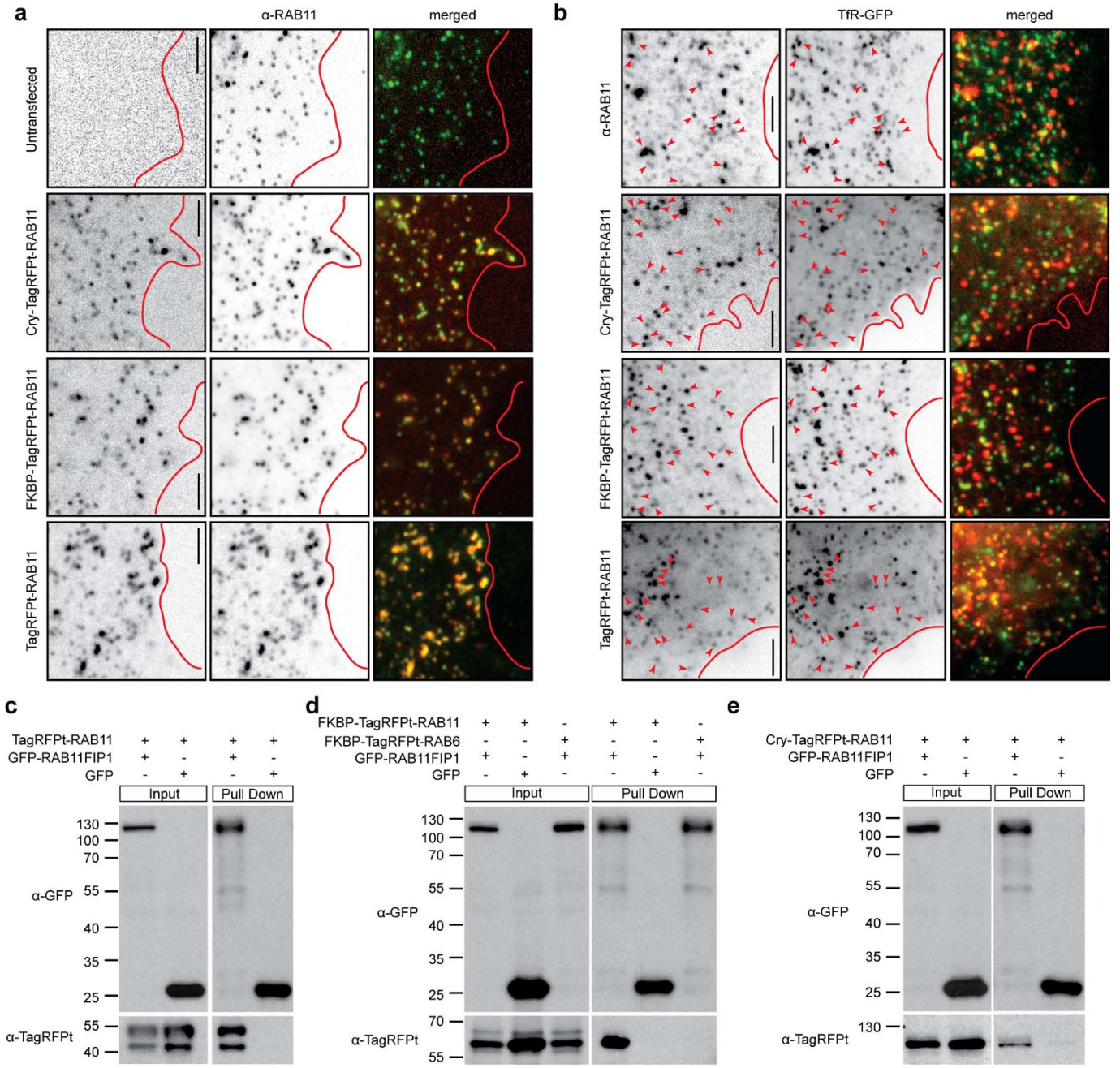

Extended Data Figure 6 | RAB11 fusion constructs are recognized by the RAB11 antibody, partially co-localize with transferrin receptors and interact with RAB11FIP1. **a**, Images of untransfected cells or cells transfected with CRY–RAB11, FKBP–RAB11 or tagRFPt–RAB11, co-stained with anti-RAB11 antibody (inverted contrast). Red lines indicate cell outline. Scale bar, 2.5 μm. **b**, Images of cells transfected with TfR-GFP only, or co-transfected with CRY–RAB11, FKBP–RAB11 or tagRFPt–RAB11 (inverted contrast). Red lines indicate cell outline. Scale bar, 2.5 μm. **c**–**e**, GFP pull-down assays with lysates of HEK cells expressing GFP or GFP–RAB11FIP1 together with tagRFPt–RAB11 (**c**), FKBP–RAB11 or FKBP–tagRFPt–RAB6 (**d**) or CRY–RAB11 (**e**) were analysed by western blotting using antibodies against tagRFPt and GFP.

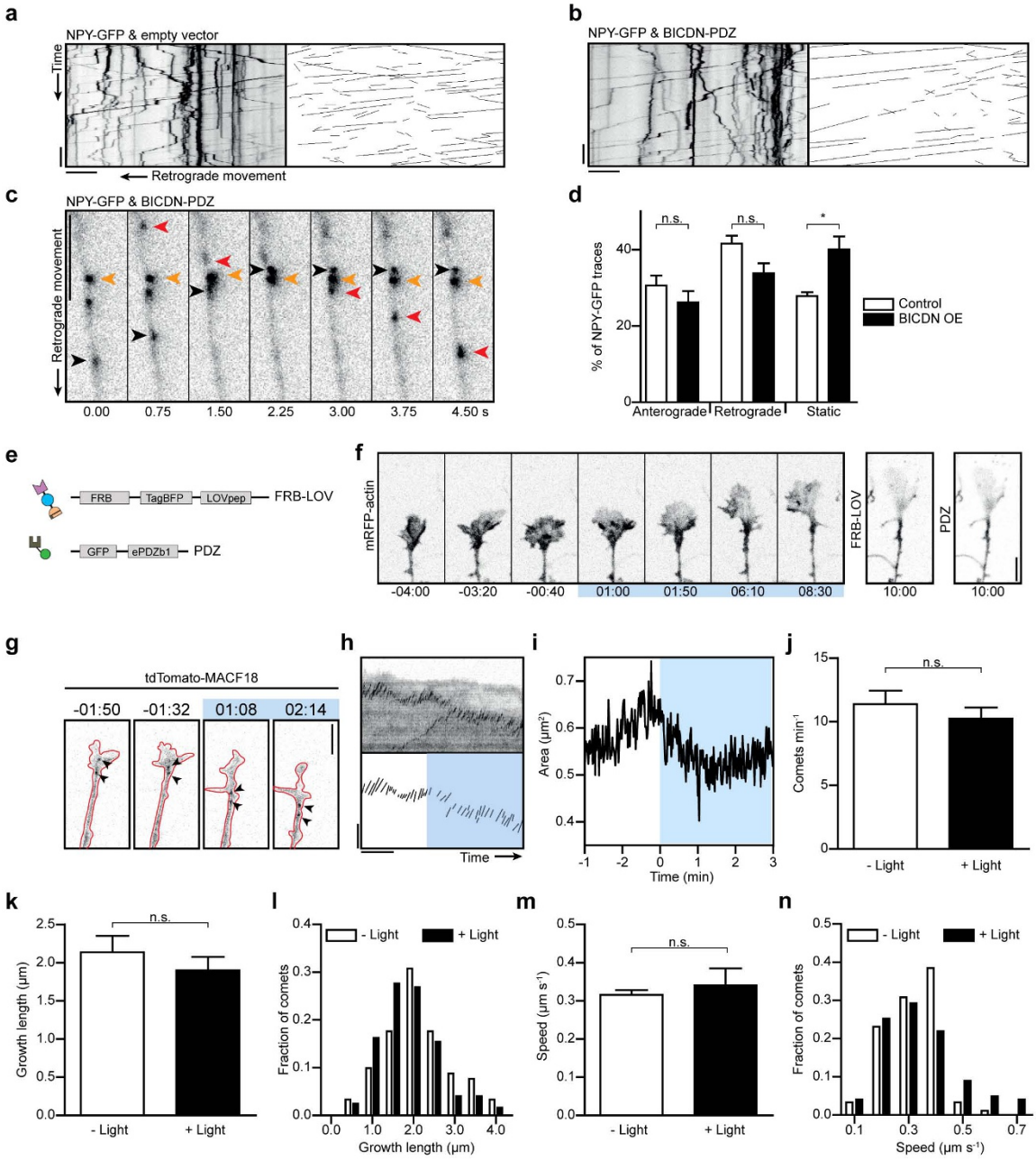

Extended Data Figure 7 | BICDN overexpression does not significantly inhibit dynein-based transport and the growth cone cytoskeleton is not affected by light-induced recruitment of BICDN to recycling endosomes. **a**, **b**, Left: kymograph of dense-core vesicles motility in an axon expressing neuropeptide Y (NPY) fused to GFP (NPY–GFP) and empty vector (**a**) or BICDN–PDZ (**b**) (inverted contrast), representative of $n = 5$ and $n = 10$ axons, respectively. Right: corresponding binary image of traces used for further analysis of anterograde and retrograde movements. Scale bars, 5 µm and 10 s. **c**, Position of dense-core vesicles along an axon expressing NPY–GFP and BICDN–PDZ. Single coloured arrowheads point to the same vesicle, highlighting retrograde (red), anterograde (black) and non-moving (orange) vesicles. Scale bar, 5 µm. **d**, Quantification of the percentage of static, anterograde and retrograde moving vesicles from kymographs shown in **a** and **b** in axons with ($n = 10$) or without ($n = 5$) BICDN–PDZ overexpression. Graph shows mean ± s.e.m., $*P > 0.05$, one-way ANOVA and Bonferroni's multiple comparison test. **e**, A fusion of FRB, tagBFP and LOVpep (FRB–LOV) and a fusion of GFP and ePDZb1 (PDZ) were expressed in neurons. After blue-light illumination, LOVpep undergoes a conformational change, allowing binding of PDZ to FRB–LOV. **f**, Actin dynamics in growth cones coexpressing mRFP–actin along with the constructs shown in **e**, in response to light-induced heterodimerization of FRB–LOV and PDZ, representative of $n = 5$ growth cones. The blue box indicates the interval of blue-light illumination. Scale bar, 5 µm. **g**, Imaging of growing microtubule (MT) plus ends using tdTomato-MACF18 shows the dynamics of microtubule plus-ends in growth cones before and during blue-light illumination in neurons co-expressing FKBP–RAB11, FRB–LOV and BICDN–PDZ. Red line indicates cell outline, arrowheads point at plus-ends. Scale bar, 5 µm. **h**, Kymograph of MACF18 comets of the growth cone shown in **g** and binarized traces used for analysis, representative of $n = 4$ growth cones. Blue box indicates blue-light illumination interval. Scale bars, 5 µm and 1 min. **i**, Area measurement of growth cone shown in **g** before and during blue-light illumination. **j**, Quantification of the number of MACF18 comets per minute in growth cones before and during blue-light illumination ($n = 4$ neurons). Graph shows mean ± s.e.m. Paired two-tailed *t*-test, $n = 4$ cells. **k**, Quantification of the growth length of MACF18 comets in growth cones before and during blue-light illumination ($n = 4$ neurons). Graph shows mean ± s.e.m. Paired two-tailed *t*-test, $n = 4$ cells. **l**, Distribution of fraction of MACF18 comets per growth length in bins of 0.5 µm ($n = 214$ traces). **m**, Quantification of the growth speed of MACF18 comets in growth cones before and during blue-light illumination ($n = 4$ neurons). Graph shows mean ± s.e.m. Paired two-tailed *t*-test, $n = 4$ cells. **n**, Distribution of fraction of MACF18 comets per growth speed in bins of 0.1 µm s^{-1} ($n = 214$ traces).

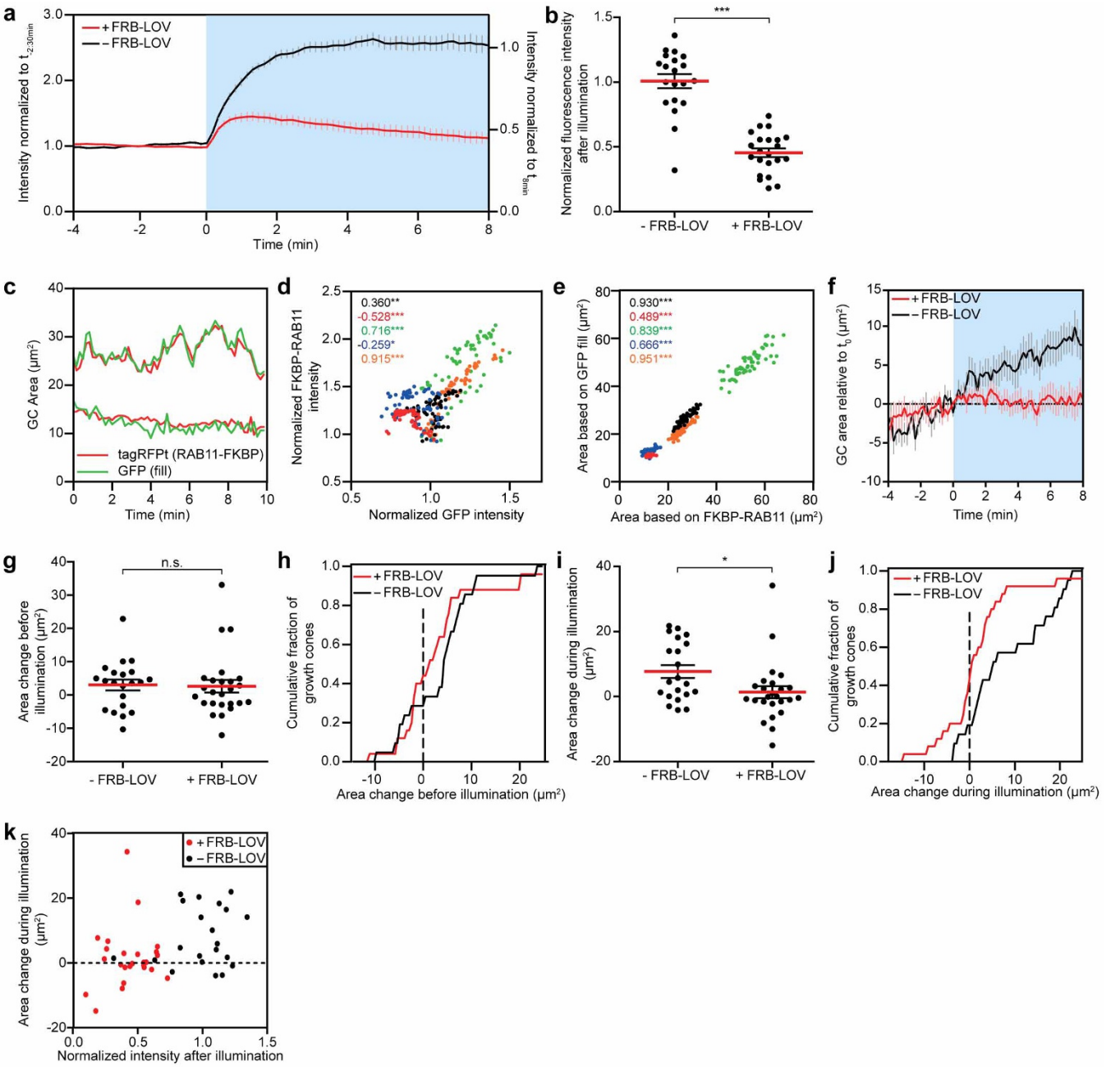

Extended Data Figure 8 | Intensity rescaling and accurate growth cone area measurements based on RAB11 fluorescence. **a**, Mean intensity of growth cone FKBP–RAB11 fluorescence from neurons expressing BICDN–PDZ in the absence (black, $n = 21$) or presence of FRB–LOV (red, $n = 25$) normalized to the intensity before ($t_{-2:30\ min}$) (left axis) and rescaled relatively to the intensity of –LOV growth cones at $t_{8\ min}$ (right axis). Blue box indicates blue-light illuminated interval. Graph shows mean ± s.e.m. **b**, Quantification of FKBP–RAB11 fluorescence intensity in the same neurons as shown in **a** after 8 min of blue-light illumination, normalized to the average fluorescence at $t_{8\ min}$ in control neurons. Graph shows mean ± s.e.m., $^{***}P < 0.0001$, Mann–Whitney test. **c**, Area measurements of two representative growth cones from neurons expressing FKBP–RAB11, FRB–LOV, BICDN–PDZ and soluble GFP over time. Representative of five growth cones (shown in **d** and **e**). **d**, Normalized tagRFPt-RAB11 intensity of five growth cones as in **c** plotted against their normalized GFP intensity. Intensity values are averaged over the first five frames per growth cone. Pearson correlation coefficient (r) for each growth cone is indicated in top left corner. Same colour indicates measurements of the same growth cone. **e**, FKBP–RAB11-based area measurements plotted against GFP-based area measurements of the same growth cones as in **d**. Pearson correlation coefficient (r) for each growth cone is indicated in top left corner. Same colour indicates measurements of the same growth cone. **f**, Traces of growth cone area measurements based on FKBP–RAB11 signal in the absence ($n = 25$, red trace) and presence of FRB–LOV ($n = 21$, black trace) in growth cones before and during blue-light illumination (see Methods). Graph shows mean ± s.e.m. Blue box indicates blue light-exposed interval. **g**, Quantification of the area increase in the absence and presence of FRB–LOV in growth cones during blue-light illumination (−4 to 0 min).Values per growth cone are averaged over three frames. Graph shows mean ± s.e.m. $P = 0.4145$ (n.s., not significant), Mann–Whitney test. **h**, Cumulative histogram showing the fraction of growth cones with area shrinkage or growth (left or right of dashed line, respectively) before blue-light illumination (−4 to 0 min). Values per growth cone are averaged over three frames. **i**, Quantification of the area change of −FRB–LOV and +FRB–LOV growth cones during blue-light illumination (0 to 8 min). Values per growth cone are averaged over three frames. Graph shows mean ± s.e.m., $^{*}P = 0.0206$, Mann–Whitney test. **j**, Cumulative histogram showing the fraction of growth cones with area shrinkage or growth (left or right of dashed line, respectively) during blue-light illumination (0–8 min). Values per growth cone are averaged over three frames. **k**, Scatter plot showing net growth during blue-light illumination and normalized fluorescence intensity after blue-light illumination per +FRB-LOV (red) or −FRB-LOV (black) growth cone.